

# Quantum Multicritical Phenomena in Disordered Weyl Semimetal

Xunlong Luo,<sup>1,2</sup> Baolong Xu,<sup>1,2</sup> Tomi Ohtsuki,<sup>3</sup> and Ryuichi Shindou<sup>1,2,\*</sup>

<sup>1</sup>International Center for Quantum Materials, Peking University, Beijing 100871, China

<sup>2</sup>Collaborative Innovation Center of Quantum Matter, Beijing 100871, China

<sup>3</sup>Department of Physics, Sophia University, Chiyoda-ku, Tokyo 102-8554, Japan

(Dated: December 14, 2024)

Three-dimensional Weyl semimetal such as layered Chern insulator exhibits a rich variety of quantum phase transitions induced by disorders. Based on numerical calculations of localization length, density of states and critical conductance distribution, we first show that a localization-delocalization transition between a Chern insulator (CI) phase with a finite zero-energy density of states (zDOS) and a diffusive metal (DM) phase belongs to an ordinary 3D unitary class. Meanwhile, a localization-delocalization transition between the Chern insulator phase with zero zDOS and a renormalized Weyl semimetal (WSM) phase turns out to be a direct phase transition whose critical exponent  $\nu = 0.80 \pm 0.01$ . We interpret these numerical results by a renormalization group analysis on a quantum multicritical phase transition among CI, DM and WSM phases.

*Introduction.*— A family of quantum matters called as Weyl semimetal [1, 2] have been recently discovered in a number of experimental materials [3–6], which show non-trivial magnetotransport properties [7–9] as a consequence of the chiral anomaly in 3+1 dimension. Besides its novel magnetotransport property, a Weyl semimetal exhibits an intriguing quantum phase transition in the presence of moderate disorder strength; a quantum phase transition between renormalized Weyl semimetal (WSM) and diffusive metallic (DM) phases [10–32]. To clarify a critical nature of this quantum phase transition, prototypical tight-binding models [24–27, 30–32] for magnetic Weyl semimetal with disorders have been studied numerically, revealing rich varieties of quantum phase transitions including non-Anderson type transitions among WSM, DM and (layered) Chern insulator (CI) phases. Thereby, the critical property in the WSM-DM quantum phase transition has been extensively studied and novel scaling properties of density of states (DOS) [10, 12, 15, 20–22, 25, 27, 31] and zero-energy conductivity [15, 21, 25] as well as their interplay with rare-event states [17, 30] have been discussed. Meanwhile, very few works have been addressed to critical properties associated with a transition between CI and DM phases and that between CI and WSM phases.

In this Letter, we clarify critical properties of the quantum phase transition lines between CI and DM phases and that between CI and WSM phases, by combining a numerical study of localization length, DOS, and two-terminal conductance with a renormalization group study of a quantum multicritical point among CI, DM and WSM phases. For a transition between CI and DM phases, we show that a mobility edge and a band edge (red and yellow curves in Fig. 1 respectively) are distinct in a phase diagram, dictating the presence of a CI phase with finite zero-energy density of states (zDOS). A localization-delocalization transition between the CI with finite zDOS and DM phase belongs to the ordinary 3D unitary class [33–38]. Around a transition point be-

tween CI with zero zDOS and CI with finite zDOS, DOS for different disorder strength and single-particle energy are shown to be well fitted into a single-parameter scaling function with a critical exponent  $\nu = 1$  and dynamical exponent  $z = 1$ . For the transition between CI and WSM phases, we show that the transition is direct and the critical exponent  $\nu$  is evaluated as 0.80 [0.79,0.81] by the numerical calculation of the localization length. We interpret these numerical results by renormalization group analyses for the quantum multicritical point among CI, DM and WSM phases.

*Model and Multicritical Quantum Phase Transition*— We numerically studied a two-orbital tight-binding model on a cubic lattice [24–27]. The model is a layered Chern insulator (LCI), which consists of two-dimensional Chern insulator in the  $x$ - $y$  plane with interlayer couplings along the  $z$ -direction. In the two-orbital model, we set a half electron filling (one band occupied, the other empty in the clean limit), and change an interlayer coupling strength (which we call  $\beta$  henceforth [39]). When the coupling strength exceeds a critical value  $\beta_c$ , the two energy bands form pairs of linearly dispersive band-touching points (‘Weyl’ points) at the Fermi level. An electronic phase for  $\beta > \beta_c$  is referred to as Weyl semimetal (WSM) phase, and a phase with an energy gap for  $\beta < \beta_c$  as Chern insulator (CI) phase. At the critical point, a low-energy effective electronic Hamiltonian takes the following form,

$$\mathcal{H}_{\text{eff}} = \int d^2\mathbf{x}_\perp dx_z \psi^\dagger(\mathbf{x}) \left\{ -iv(\partial_x \sigma_x + \partial_y \sigma_y) + ((-i)^2 b_2 \partial_z^2 - m) \sigma_z \right\} \psi(\mathbf{x}). \quad (1)$$

$\psi^\dagger(\mathbf{x})$  and  $\psi(\mathbf{x})$  denote a two-component slowly-varying fermion field obtained from the  $\mathbf{k} \cdot \mathbf{p}$  expansion around degenerate Weyl points at  $\beta = \beta_c$ .  $m$  corresponds to the interlayer coupling strength,  $m = \beta - \beta_c$ . For  $m < 0$ , the effective Hamiltonian has a finite energy gap (CI phase). For  $m > 0$ , the Hamiltonian has a pair of the Weyl points in the momentum space,  $(p_x, p_y, p_z) = (0, 0, \pm \sqrt{m/b_2})$ .

Effects of various types of disorders on the critical theory in eq. (1) can be captured by renormalization group (RG) analyses [31, 39]. A tree-level scaling argument dictates that a scaling dimension of the most relevant disorder is  $-1/2$ . This suggests the presence of a non-trivial fixed point with a finite critical disorder strength, below which the disorder is irrelevant, while above which the disorder blows up to a larger value. A perturbative RG equation takes a form of coupled equations of the mass term  $m$  and properly normalized (chemical-potential type) disorder strength  $\bar{\Delta}_0$  [31, 39];

$$\frac{dm}{dl} = m(1 - 2\bar{\Delta}_0), \quad (2)$$

$$\frac{d\bar{\Delta}_0}{dl} = -\frac{1}{2}\bar{\Delta}_0 + 2\bar{\Delta}_0^2. \quad (3)$$

The equation has a trivial fixed point in the clean limit  $(\bar{\Delta}_0, m) = (0, 0)$  (FP0) and the nontrivial fixed point at finite critical disorder strength  $(\bar{\Delta}_0, m) = (\Delta_c, 0)$  with  $\Delta_c = 1/4$  (FP1). The critical phase described by eq. (1) is stable up to the critical disorder strength  $(\bar{\Delta}_0 < \Delta_c)$ , above which a system enters a diffusive metallic (DM) phase  $(\bar{\Delta}_0 > \Delta_c)$ . The critical phase in  $0 < \bar{\Delta}_0 < \Delta_c$  and  $m = 0$  intervenes WSM and CI phases. The fixed point at  $(\bar{\Delta}_0, m) = (\Delta_c, 0)$  plays role of a quantum multicritical point among WSM, CI and DM phases (inset of

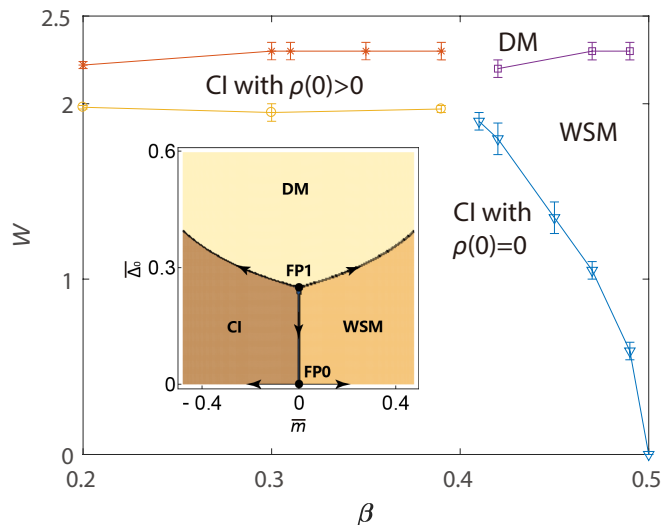


FIG. 1. (color online) Phase diagram for disordered Weyl semimetal. The horizontal axis indicates the coupling between the layers, while the vertical axis indicates the strength of disorder. Red, purple and blue lines are boundaries between CI and DM, between WSM and DM and between CI and WSM respectively. These boundaries are determined by the localization length calculation. Yellow line is a boundary between CI phase with zero zero-energy density of states (zDOS) and CI phase with finite zDOS, which is determined by the density of states calculation. Inset: Phase diagram determined by perturbative renormalization group analyses [31, 39].

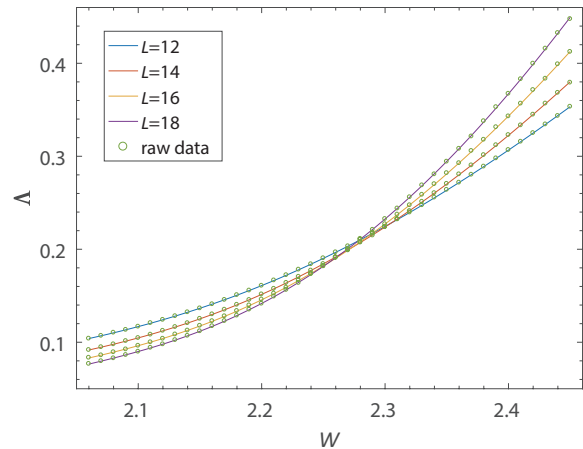


FIG. 2. (color online)  $\Lambda \equiv \lambda/L$  as a function of disorder strength for  $\beta = 0.2$  with a cross section size  $L = 12, 14, 16, 18$ . The circle is the raw data of  $\Lambda$  and the four curves are the fitting result with the Taylor-expansion orders:  $(m_1, m_2, n_1, n_2) = (2, 0, 3, 1)$  (see the text).

Fig. 1). In the phase diagram, the quantum multicritical point has three branches. Critical natures of the non-Anderson type quantum phase transition between WSM and DM phases have been previously studied by DOS scaling analyses [25, 27]. In the followings, we clarify critical properties of the other two branches, a quantum phase transition line between CI and DM phases and that between CI and WSM phases.

*Critical Exponent for CI-DM Branch*—To clarify a nature of the phase transition between CI and DM phases, we include in LCI a short-ranged on-site disorder potential, whose strength is denoted by  $W$  henceforth, and calculate a quasi-one dimensional localization length  $\lambda$  of eigenstates at the Fermi level ( $E = 0$ ) by transfer matrix method. We use a quasi-one-dimensional geometry with a square cross-section  $L_x = L_y = L$ , to calculate the localization length along the  $z$ -direction with variable length  $L_z$ . For longer  $L_z$ , smaller is the standard deviation  $\sigma_\Lambda$  of a normalized localization length  $\Lambda \equiv \lambda/L$  [40, 41]. We terminate the transfer matrix calculation, when a precision  $\sigma_\Lambda/\Lambda$  reaches 0.1% for  $L = 12, 14$  and 0.2 % for  $L = 16, 18$ . Fig. 2 shows  $\Lambda$  as a function of  $W$  for different  $L$ . The scale-invariant behavior of  $\Lambda$  indicates a localization-delocalization phase transition induced by  $W$ .

To determine a critical disorder strength  $W_c$  and critical exponent of the phase transition, we use polynomial fitting method. We assume that the normalized localization length  $\Lambda$  depends on disorder strength  $W$  and system size  $L$  through a universal function of only two scaling variables,  $F(\phi_1, \phi_2)$  [42, 43].  $\phi_1$  is a relevant scaling variable with positive exponent  $\alpha_1 \equiv 1/\nu$  and  $\phi_2$  is an irrelevant scaling variable with the largest negative expo-

$m_1$	$m_2$	GOF	$W_c$	$\nu$	$-y$
2	0	0.27	2.21[2.19,2.23]	1.34[1.23,1.53]	2.6[2.0,3.4]
3	0	0.82	2.22[2.18,2.23]	1.27[1.18,1.48]	3.0[2.0,4.0]
2	1	0.29	2.22[2.19,2.23]	1.31[1.22,1.52]	3.0[2.1,3.9]
3	1	0.81	2.22[2.18,2.23]	1.26[1.18,1.48]	2.9[2.0,3.8]

TABLE I. Polynomial fitting results for the localization-delocalization transition between CI and DM phases at  $\beta = 0.2$  with  $(n_1, n_2) = (3, 1)$ . The goodness of fit (GOF), critical disorder  $W_c$ , critical exponent  $\nu \equiv 1/\alpha_1$ , largest irrelevant exponent  $y$  are shown for different orders of the Taylor expansion  $(m_1, m_2)$ . A value of  $\Lambda$  at the critical point is 0.14 [0.11, 0.16]. Error bar in the square bracket denotes the 95% confidence interval.

nent  $\alpha_2 \equiv y$ .  $\Lambda$  depends on  $W$  and  $L$  through the scaling variables,  $\phi_j \equiv u_j(\omega)L^{\alpha_j}$  where  $\omega \equiv (W - W_c)/W_c$ . By definition,  $u_1(\omega = 0) = 0$  and  $u_2(\omega = 0) \neq 0$ . Assuming that  $\omega$  is small and  $L$  is large enough, we Taylor-expand the universal function in small  $\phi_1$  and  $\phi_2$  and  $u_j(\omega)$  in small  $\omega$ ;  $\Lambda = F(\phi_1, \phi_2) = \sum_{j_1=0}^{n_1} \sum_{j_2=0}^{n_2} a_{j_1, j_2} \phi_1^{j_1} \phi_2^{j_2}$ ,  $u_i(\omega) = \sum_{j=0}^{m_i} b_{i, j} \omega^j$ . For a given set of  $(n_1, n_2, m_1, m_2)$ , we minimize  $\chi^2 \equiv \sum_{j=1}^{N_D} (F_j - \Lambda_j)^2 / \sigma_j^2$  in terms of  $W_c$ ,  $\alpha_1 \equiv \nu^{-1}$ ,  $\alpha_2 \equiv y$ ,  $a_{i, j}$ , and  $b_{l, m}$  with  $a_{1,0} = a_{0,1} = 1$  and  $b_{1,0} = 0$ .  $\Lambda_j$  and  $\sigma_j$  ( $j = 1, \dots, N_D$ ) are values of  $\Lambda$  and  $\sigma_\Lambda$  in Fig. 2 for a given  $L$  and  $W$ .  $j$  specifies a data point, while  $N_D$  is a number of those data points that are used for the fitting.  $F_j$  is a value of  $\Lambda$  from the polynomial fitting at the same  $L$  and  $W$ . Fittings are carried out for several different  $(n_1, n_2, m_1, m_2)$  with  $n_1, n_2, m_1 \leq 3$ ,  $m_2 \leq 2$ . Those fitting results with goodness of fit (GOF) greater than 0.1 is shown in Table. 1. We also carry out the same fitting for 1000 synthetic data sets of  $\{\Lambda_1, \dots, \Lambda_{N_D}\}$ , to determine 95% confidence interval [43].

A fit with the smallest number of parameters gives the exponent  $\nu = 1.34$  [1.23, 1.53]. The fitting is stable against the increase of the expansion orders (Table. I and [? ]). The value is consistent with  $\nu \approx 1.443$ [.437, .449] [35] for the ordinary 3D unitary class, suggesting that the localization-delocalization transition between CI and DM phases belong to the same universality class as the ordinary 3D unitary class [33–38].

*Critical Conductance for CI-DM Branch*— To reinforce the above result, we calculate a critical conductance distribution (CCD) and compare this with CCD in a reference tight-binding model whose Anderson transition is known to belong to the ordinary 3D universality class [33]. CCD generally depends only on the symmetry class and system’s geometry, but free from a system size [44]. The geometry of a system is determined by mean values of two-terminal conductances at the critical point along  $x$ ,  $y$  and  $z$  directions, i. e.  $G_x$ ,  $G_y$  and  $G_z$ . In our model,  $G_x = G_y \equiv G_\perp$ , while out-plane conductance  $G_z$  differs from the in-plane conductance  $G_\perp$ . We fine-tune  $L_z$  with fixed  $L_x = L_y = L$ , such that  $G_z$  and  $G_\perp$  at

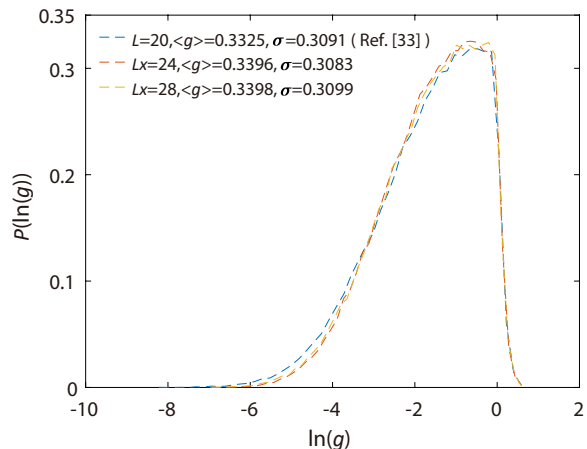


FIG. 3. (color online) Critical conductance distributions (CCD) along the  $z$ -direction of LCI model at  $W = W_c = 2.21$ ,  $\beta = 0.2$  with  $L_x = L_y = 4L_z$  (periodic boundary conditions in  $x$  and  $y$  directions).  $L_x = 24$  (red broken line) and  $L_x = 28$  (orange). CCD of the cubic U(1) tight-binding model [33] (blue) is compared with them. Each distribution include  $10^5$  samples.  $g$  is the two terminal conductance  $G_z$  in unit of  $e^2/h$ .

the critical point become identical (very close) to those calculated from the reference tight-binding model [33]. For the critical point shown in Fig. 2,  $L/L_z = 4$  realizes this. Fig. 3 shows a distribution of  $G_z$  at the critical point with different  $L$  with fixed  $L/L_z = 4$ . The distributions are almost identical to the CCD in the reference tight-binding model. This in combination with the critical exponent concludes that the localization-delocalization transition for the CI-DM branch belong to the ordinary 3D unitary class.

*Density of States for CI-DM Branch*— The above observation indicates that, unlike in the critical line between DM and WSM phases [10–30], zDOS is finite at the localization-delocalization transition between DM and CI phases. To confirm this, we calculate DOS in disordered LCI with cubic geometry ( $L_x = L_y = L_z = L$ ) by kernel polynomial expansion method [45]. We set  $L$  to be 100 and/or 200 and the order of the Chebyshev polynomial expansion to a few thousands. Considering a self-averaging nature of DOS, we average the calculated DOS over two ( $L = 200$ ) and four ( $L = 100$ ) different disorder realizations. On increasing the disorder strength  $W$ , we found that the gapped Chern insulator phase acquires a finite zDOS  $\rho(0)$  below the localization-delocalization transition point,  $\rho(0) \propto |W - W_{c,1}|^\phi$  with  $\phi = 1.99 \pm 0.03$  and  $W_{c,1} < W_c$  (Fig. 4 and Fig. 1). The zero-energy eigenstates are localized at  $W_{c,1} < W < W_c$ . Firstly, this concludes that zDOS at the localization-delocalization transition point for the CI-DM branch is finite and dynamical exponent associated with this transition is 3. Note also that, within the self-consistent Born approx-

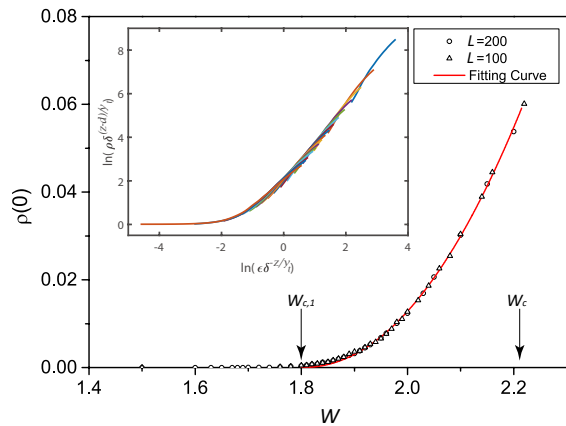


FIG. 4. (color online) zDOS  $\rho(0)$  as a function of disorder for  $\beta = 0.2$ . The data points are fitted by a curve of  $\rho(0) \propto \delta^\phi$  with  $\phi = 1.99 \pm 0.03$ . Inset: Single-parameter scaling of DOS  $\rho(\mathcal{E})$  for  $\beta = 0.2$ , different  $W (> W_{c,1})$  and single-particle energy  $\mathcal{E}$  with  $\rho(\mathcal{E}) > 0.008$ . We use  $\rho(\mathcal{E}) = \delta^{(d-z)\nu} \Psi(\delta^{-z\nu} \mathcal{E})$  with  $\delta \equiv |W - W_{c,1}|/W_{c,1}$ ,  $d = 3$ ,  $z = 1$  and  $\nu = 1$  [15, 39].

$n$	$m$	GOF	$\beta_c$	$\nu$
4	2	0.79	0.4716[0.4715,0.4716]	0.8008[0.7947,0.8068]
5	2	0.95	0.4716[0.4715,0.4716]	0.8002[0.7943,0.8069]
4	3	0.81	0.4716[0.4715,0.4717]	0.8097[0.7964,0.8225]
5	3	0.97	0.4716[0.4715,0.4716]	0.8124[0.7990,0.8261]

TABLE II. Polynomial fitting results with goodness of fit greater than 0.1 are shown with the 95% confidence interval for critical  $\beta$  ( $\beta_c$ ) and critical exponent  $\nu$ .

imation, the exponent  $\phi$  associated with  $\rho(0)$  is evaluated as  $1/2$  [25], while our numerical observation ( $\phi \simeq 2$ ) clearly deviates from this. Meanwhile, the DOS for different (but small) single-particle energy  $\mathcal{E}$  and disorder strength  $W > W_{c,1}$  can be well fitted into a same single-parameter scaling function (inset of Fig. 4).

The critical properties for the CI-DM branch is distinct from that for the WSM-DM branch. This is consistent with the RG flow around the non-trivial fixed point with finite disorder (‘FP1’ in the inset of Fig. 1). Around FP1, the mass term is a relevant scaling variable, so that the critical properties for the CI-DM branch are controlled by saddle-point fixed points at finite  $m (< 0)$  and that for the WSM-DM branch is by a saddle-point fixed point at finite  $m (> 0)$ . Especially, the single-parameter scaling in Fig. 4,  $\rho(E) \sim \delta^{(d-z)\nu} \Psi(E\delta^{-z\nu})$  [15, 25], suggests that the DOS scaling around the phase boundary between CI with zero zDOS and CI with finite zDOS is controlled by a saddle-point fixed point at finite  $m < 0$  [39]. From the fitting, we evaluate  $\nu = 1$  and  $z = 1$  for this (postulated) saddle-point fixed point.

*Critical Exponent for CI-WSM Branch.*— To clarify a critical nature of phase transition between CI with zero zDOS and WSM phases, we calculate a localization length along the  $z$ -direction at  $E = 0$ . We fix  $W$

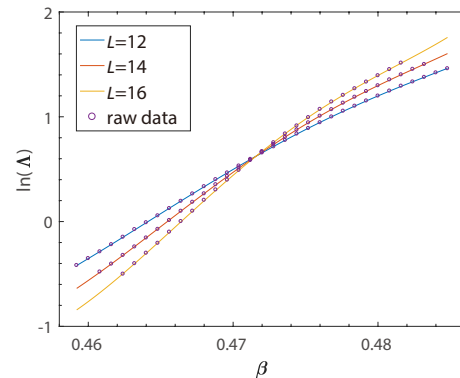


FIG. 5. (color online)  $\ln(\Lambda)$  as a function of  $\beta$  at  $W = 1$  for the CI-WSM transition with cross-section size  $L = 12, 14, 16$ . The circle is the raw data and the curves are the fitting result with the expansion orders  $(n, m) = (4, 2)$  (see the text).

and calculate  $\lambda$  by changing  $\beta$ . The calculation is terminated when the precision of  $\Lambda$  reaches 0.2% for  $L=12, 14$  and 0.4% for  $L=16$ . As in Fig. 5, curves of  $\Lambda$  for different  $L$  intersect almost at the same critical  $\beta$ . We thus use the polynomial fitting without the finite-size correction;  $\Lambda = F(\phi_1)$ . Table II shows a list of the critical exponent  $\nu$  and critical mass  $\beta_c$  with different expansion orders;  $F(\phi_1) = \sum_{j=0}^n a_j \phi_1^j$  with  $\phi_1(\omega) = \sum_{j=1}^m b_j \omega^j$ . The fitting with the smallest number of parameters gives  $\nu = 0.80$  [0.79, 0.81], which are stable against the increase of the Taylor expansion orders.

According to the RG analyses, the critical property for CI-WSM branch is determined by the fixed point in the clean limit (‘FP0’ in inset of Fig. 1). Around FP0, the mass term is a relevant scaling variable with its scaling dimension  $+1$ :  $[m] = +1$ . The critical theory given by eq. (1) at  $m = 0$  has a linear dispersion along the  $x$ - $y$  plane, and a quadratic dispersion along the  $z$ -direction. This leads to an anisotropic scaling:  $[x_z] = -1/2$ ,  $[x_\perp] = -1$ , dictating that a characteristic length scale along  $z$ -direction and that along the in-plane direction are scaled with the mass term differently,  $\xi_z = m^{-1/2}$ ,  $\xi_\perp = m^{-1}$ . Meanwhile,  $\xi_z = m^{-1/2}$  clearly contradicts with our precise determination of  $\nu$ .

The discrepancy may be attributed to effect of finite disorders. Though the critical line between CI and WSM phases is controlled by the clean-limit fixed point, any finite small disorder could average out the spatial anisotropy in the scaling property. When a characteristic length scale  $\xi$  is defined as a cubic root of a characteristic volume, the scaling exponent of such  $\xi$  with respect to  $m$  can be around our numerical observation,  $\nu_{\text{th}} = \frac{1}{3}(\frac{1}{2} + 1 + 1) = 0.833 \dots$ . Nonetheless, we cannot exclude a possibility that the discrepancy simply stems from a crossover phenomenon between FP1 and FP0 either. In fact, the perturbative RG equations given by eqs. (2) and (3) dictate that the exponent  $\nu$  at FP1 and

FP0 is +1 and +1/2 respectively, while our numerical evaluation places between these two values.

*Conclusion.*— In this Letter, we clarify the critical nature of the localization-delocalization transition between CI and DM phases and that between CI and WSM phases in disordered layered Chern insulator. The results are consistent with RG analyses for the quantum multicritical point among DM, WSM and CI phases. The same critical behaviors are expected for the ordinary insulator-WSM-DM tricritical point [24–27].

This work (XL, BX, RS) was supported by NBRP of China Grants No. 2014CB920901, No. 2015CB921104, and No. 2017A040215. TO was supported by JSPS KAK-ENHI Grant No. JP15H03700 and JP17K18763.

## SUPPLEMENTAL MATERIAL

### Tight-Binding Cubic-Lattice Model for Weyl Semimetal

We use the same two-orbital tight-binding model on a cubic lattice as studied previously [24–27, 31, 32]. The model consists of an  $s$  orbital and a  $p = p_x + ip_y$  orbital on each cubic lattice site ( $\mathbf{x}$ );

$$\begin{aligned} \mathcal{H} = & \sum_{\mathbf{x}} \left\{ (\epsilon_s + v_s(\mathbf{x})) c_{\mathbf{x},s}^\dagger c_{\mathbf{x},s} + (\epsilon_p + v_p(\mathbf{x})) c_{\mathbf{x},p}^\dagger c_{\mathbf{x},p} \right\} \\ & + \sum_{\mathbf{x}} \left\{ - \sum_{\mu=1,2} (t_s c_{\mathbf{x}+\mathbf{e}_\mu,s}^\dagger c_{\mathbf{x},s} - t_p c_{\mathbf{x}+\mathbf{e}_\mu,p}^\dagger c_{\mathbf{x},p}) \right. \\ & + t_{sp} (c_{\mathbf{x}+\mathbf{e}_1,p}^\dagger - c_{\mathbf{x}-\mathbf{e}_1,p}^\dagger - i c_{\mathbf{x}+\mathbf{e}_2,p}^\dagger + i c_{\mathbf{x}-\mathbf{e}_2,p}^\dagger) c_{\mathbf{x},s} \\ & \left. - t'_s c_{\mathbf{x}+\mathbf{e}_3,s}^\dagger c_{\mathbf{x},s} - t'_p c_{\mathbf{x}+\mathbf{e}_3,p}^\dagger c_{\mathbf{x},p} + \text{H.c.} \right\}, \quad (4) \end{aligned}$$

$\epsilon_s$ ,  $\epsilon_p$  and  $v_s(\mathbf{x})$ ,  $v_p(\mathbf{x})$ , are atomic energies for the  $s$ ,  $p$  orbital and on-site disorder potential of the  $s$ ,  $p$  orbital, respectively. The disorder potentials are uniformly distributed within  $[-W/2, W/2]$  with identical probability distribution.  $t_s$ ,  $t_p$ , and  $t_{sp}$  are intralayer transfer integrals between  $s$  orbitals of nearest neighboring two sites, that between  $p$  orbitals, and that between  $s$  and  $p$  orbitals, respectively, while  $t'_s$  and  $t'_p$  are interlayer transfer integrals.  $\mathbf{e}_\mu$  ( $\mu = 1, 2$ ) are primitive translational vectors within a square-lattice plane.  $\mathbf{e}_3$  is a primitive translational vector connecting neighboring square-lattice layers. Without the interlayer transfers, the electron model in the clean limit at half electron filling (one electron filling per cubic lattice site) is in either one of the two (layered) Chern band insulator phases ( $0 < \epsilon_s - \epsilon_p < 4(t_s + t_p)$ ,  $-4(t_s + t_p) < \epsilon_s - \epsilon_p < 0$ ) or in the ordinary insulator phase ( $4(t_s + t_p) < |\epsilon_s - \epsilon_p|$ ). In this paper, we take  $\epsilon_s - \epsilon_p = -2(t_s + t_p)$ ,  $t_s = t_p > 0$ , and  $t_{sp} = 4t_s/3$ . A larger interlayer coupling induces a phase transition from the layered Chern insulator phase to Weyl semimetal phase. In this paper, we take  $t'_s = -t'_p > 0$ .

For  $\beta \equiv (t'_s - t'_p)/[2(t_s + t_p)]$  greater than 1/2, a fourier-transformed tight-binding Hamiltonian has three pairs of Weyl nodes at  $\mathbf{k} = (\pi, \pi, \pm k_0)$ ,  $(0, \pi, \pi \pm k_0)$  and  $(\pi, 0, \pi \pm k_0)$  with  $\cos k_0 \equiv \frac{1}{2\beta}$ . In a clean-limit phase diagram subtended by  $\beta$ , a quantum critical point ( $\beta = 1/2$ ) intervenes the Chern insulator phase ( $\beta < 1/2$ ) and a Weyl semimetal phase with three pairs of Weyl nodes ( $\beta > 1/2$ ).

### Renormalization Group Analyses for Low-Energy Effective Electron Hamiltonian with Disorders

At the quantum critical point, three pairs of Weyl nodes annihilate at the high symmetric  $\mathbf{k}$  points;  $\mathbf{k} = (\pi, \pi, 0)$ ,  $(\pi, 0, \pi)$  and  $(0, \pi, \pi)$  respectively. Each pair annihilation is described by the following two by two effective Hamiltonian, which is obtained from the  $\mathbf{k} \cdot \mathbf{p}$  expansion around these high symmetric  $\mathbf{k}$  points;

$$\mathbf{H}_{\text{eff}}(\mathbf{p}) = v(p_1 \boldsymbol{\sigma}_1 + p_2 \boldsymbol{\sigma}_2) + (b_2 p_3^2 - m) \boldsymbol{\sigma}_3. \quad (5)$$

Here  $\mathbf{p} \equiv (p_1, p_2, p_3)$  denotes a crystal momentum measured from the three high symmetric  $\mathbf{k}$  points. Velocities along the  $x$  and  $y$  directions are same due to the  $C_4$  rotational symmetry. For  $m < 0$ , the effective Hamiltonian is gapped for the half-filling case (Chern insulator phase), while, for  $m > 0$ , the Hamiltonian has a pair of Weyl nodes at  $(p_1, p_2, p_3) = (0, 0, \pm \sqrt{m/b_2})$ .

Effect of disorders on the quantum critical point can be studied by the following replicated effective action [37, 46],

$$\begin{aligned} Z = & \int d\psi_\alpha^\dagger \psi_\alpha e^{-S}, \quad S = S_0 + S_1, \\ S_0 \equiv & \int d\tau \int d^2 \mathbf{x}_\perp dx_3 \psi_\alpha^\dagger(\mathbf{x}, \tau) \left\{ a \partial_\tau - iv(\partial_1 \boldsymbol{\sigma}_1 + \partial_2 \boldsymbol{\sigma}_2) \right. \\ & \left. + ((-i)^2 b_2 \partial_3^2 - m) \boldsymbol{\sigma}_3 \right\} \psi_\alpha(\mathbf{x}, \tau) \quad (6) \\ S_1 \equiv & -\frac{\Delta_0}{2} \int d\tau \int d\tau' \int d^3 \mathbf{x} (\psi_\alpha^\dagger \psi_\alpha)_{\mathbf{x},\tau} (\psi_\beta^\dagger \psi_\beta)_{\mathbf{x},\tau'} \\ & - \frac{\Delta_3}{2} \int d\tau \int d\tau' \int d^3 \mathbf{x} (\psi_\alpha^\dagger \boldsymbol{\sigma}_3 \psi_\alpha)_{\mathbf{x},\tau} (\psi_\beta^\dagger \boldsymbol{\sigma}_3 \psi_\beta)_{\mathbf{x},\tau'} \\ & - \frac{\Delta_\perp}{2} \sum_{\mu=1,2} \int d\tau \int d\tau' \int d^3 \mathbf{x} (\psi_\alpha^\dagger \boldsymbol{\sigma}_\mu \psi_\alpha)_{\mathbf{x},\tau} (\psi_\beta^\dagger \boldsymbol{\sigma}_\mu \psi_\beta)_{\mathbf{x},\tau'} \quad (7) \end{aligned}$$

where a coefficient in front of  $\partial_\tau$  in  $S_0$  is for a bookkeeping purpose;  $a = 1$ . Here we have considered only short-ranged correlated on-site disorders in the low-energy effective Hamiltonian,

$$\begin{aligned} \mathcal{H}_{\text{eff}} = & \int d^3 \mathbf{x} \psi^\dagger(\mathbf{x}) \left\{ -iv(\partial_1 \boldsymbol{\sigma}_1 + \partial_2 \boldsymbol{\sigma}_2) + \right. \\ & \left. ((-i)^2 b_2 \partial_3^2 - m) \boldsymbol{\sigma}_3 + \sum_{\mu=0,1,2,3} V_\mu(\mathbf{x}) \boldsymbol{\sigma}_\mu \right\} \psi(\mathbf{x}), \quad (8) \end{aligned}$$

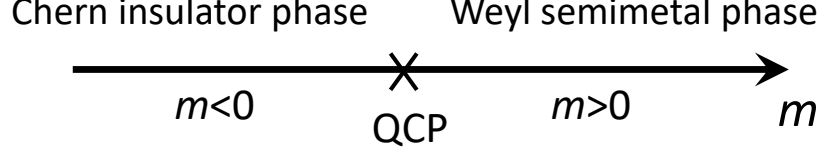


FIG. 6. (color online) Schematic phase diagram for a quantum critical point intervening layered Chern insulator phase ( $m < 0$ ) and Weyl semimetal phase ( $m > 0$ ).  $m < 0$  corresponds to  $\beta < \frac{1}{2}$  and  $m > 0$  to  $\beta > \frac{1}{2}$  in the LCI model in this paper.

with  $\langle V_\mu(\mathbf{x})V_\nu(\mathbf{x}') \rangle_{\text{imp}} = \Delta_\mu \delta_{\mu\nu} \delta^3(\mathbf{x} - \mathbf{x}')$ , and  $\Delta_1 = \Delta_2 \equiv \Delta_\perp$ . The summation over the replica indice  $\alpha$  and  $\beta$  are omitted ( $\alpha = 1, \dots, N$ ). In the perturbative derivation of renormalization group equations, we only keep those Feynman diagram contributions which survive

in the limit of  $N \rightarrow 0$ . Following Roy et. al [31], we employ a momentum-shell renormalization method, to decompose the fermion field  $\psi_\alpha$  into a slow mode ( $\psi_{\alpha,<}$ ) and a fast mode ( $\psi_{\alpha,>}$ ) in the momentum space,

$$\begin{aligned} \psi_\alpha(\mathbf{x}, \tau) &= \psi_{\alpha,<}(\mathbf{x}, \tau) + \psi_{\alpha,>}(\mathbf{x}, \tau) \\ &= \frac{1}{\sqrt{\beta V}} \sum_{i\mathcal{E}_n, \mathbf{p}}^{p_\perp < \Lambda e^{-d\tau}} e^{i\mathbf{p}\mathbf{x} - i\mathcal{E}_n\tau} \psi_\alpha(\mathbf{p}, \mathcal{E}_n) + \frac{1}{\sqrt{\beta V}} \sum_{i\mathcal{E}_n, \mathbf{p}}^{\Lambda e^{-d\tau} < p_\perp < \Lambda} e^{i\mathbf{p}\mathbf{x} - i\mathcal{E}_n\tau} \psi_\alpha(\mathbf{p}, \mathcal{E}_n). \end{aligned}$$

with  $p_\perp \equiv \{p_1^2 + p_2^2\}^{\frac{1}{2}}$ . The integration of the fast mode in the partition function leads to a renormalization of effective action for the slow mode,

$$\begin{aligned} Z &= \int d\psi_{\alpha,<}^\dagger d\psi_{\alpha,<} e^{-S_{0,<}} \int d\psi_{\alpha,>}^\dagger d\psi_{\alpha,>} e^{-S_{0,>}} e^{-S_{1,>}} \\ &\equiv Z_{0,>} \int d\psi_{\alpha,<}^\dagger d\psi_{\alpha,<} e^{-S_{0,<}} \langle e^{-S_{1,>}} \rangle_{0,>} \\ &= Z_{0,>} \int d\psi_{\alpha,<}^\dagger d\psi_{\alpha,<} e^{-S_{0,<}} e^{-\langle S_{1,>} \rangle_{0,>} + \frac{1}{2} (\langle S_{1,>}^2 \rangle_{0,>} - \langle S_{1,>} \rangle_{0,>}^2) + \dots \end{aligned} \quad (9)$$

where

$$\langle \dots \rangle_{0,>} \equiv \frac{1}{Z_{0,>}} \int d\psi_{\alpha,>}^\dagger d\psi_{\alpha,>} e^{-S_{0,>}} \dots, \quad Z_{0,>} \equiv \int d\psi_{\alpha,>}^\dagger d\psi_{\alpha,>} e^{-S_{0,>}}$$

and

$$\begin{aligned} S_{1,>} &= -\frac{\Delta_0}{2} \int d\tau \int d\tau' \int d^3\mathbf{x} \left\{ 2(\psi_{\alpha,>}^\dagger \psi_{\alpha,>})_{\mathbf{x},\tau} (\psi_{\beta,<}^\dagger \psi_{\beta,<})_{\mathbf{x},\tau'} + 2(\psi_{\alpha,<}^\dagger \psi_{\alpha,<})_{\mathbf{x},\tau} (\psi_{\beta,>}^\dagger \psi_{\beta,<})_{\mathbf{x},\tau'} \right. \\ &\quad \left. + (\psi_{\alpha,>}^\dagger \psi_{\alpha,<})_{\mathbf{x},\tau} (\psi_{\beta,>}^\dagger \psi_{\beta,<})_{\mathbf{x},\tau'} + (\psi_{\alpha,<}^\dagger \psi_{\alpha,>})_{\mathbf{x},\tau} (\psi_{\beta,<}^\dagger \psi_{\beta,>})_{\mathbf{x},\tau'} \right\} - \frac{\Delta_3}{2} \int \dots - \frac{\Delta_\perp}{2} \sum_{\mu=1,2} \int \dots \end{aligned} \quad (10)$$

$$S_{0,>(<)} = \sum_{i\mathcal{E}_n} \sum_{p_3} \sum_{p_\perp}' \psi_\alpha^\dagger(\mathbf{p}, \mathcal{E}_n) \left\{ -i\mathcal{E}_n a \boldsymbol{\sigma}_0 + v(p_1 \boldsymbol{\sigma}_1 + p_2 \boldsymbol{\sigma}_2) + (b_2 p_3^2 - m) \boldsymbol{\sigma}_3 \right\} \psi_\alpha(\mathbf{p}, \mathcal{E}_n). \quad (11)$$

The integral region over  $\mathbf{p}$  in  $S_{0,>(<)}$  is restricted within the fast mode (slow mode).  $S_{1,<}$  comprises only of the slow modes. We keep only those terms in eq. (9) which survive in the zero-replica limit ( $N \rightarrow 0$ ) [10, 12, 20, 21, 31];

$$\begin{aligned} \langle S_{1,>} \rangle_{0,>} &= -(\Delta_0 + 2\Delta_\perp + \Delta_3) \sum_{i\mathcal{E}_n} \sum_{\mathbf{p}}' h_0 i\mathcal{E}_n \psi_{\alpha,<}^\dagger(\mathbf{p}, i\mathcal{E}_n) \boldsymbol{\sigma}_0 \psi_{\alpha,<}(\mathbf{p}, i\mathcal{E}_n) \\ &\quad - (\Delta_0 - 2\Delta_\perp + \Delta_3) \sum_{i\mathcal{E}_n} \sum_{\mathbf{p}}' h_1 \psi_{\alpha,<}^\dagger(\mathbf{p}, i\mathcal{E}_n) \boldsymbol{\sigma}_3 \psi_{\alpha,<}(\mathbf{p}, i\mathcal{E}_n) \end{aligned} \quad (12)$$

with

$$h_0 = \frac{1}{V} \sum_{q_3} \sum_{\Lambda e^{-dl} < q_\perp < \Lambda} \frac{1}{\mathcal{E}_n^2 + v^2 q_\perp^2 + (b_2 q_3^2 - m)^2} = \frac{\Lambda^2 dl}{4\pi^2} \int_{-\infty}^{+\infty} \frac{dp_3}{(v\Lambda)^2 + (b_2 p_3^2 - m)^2} \equiv H_0 dl \quad (13)$$

$$h_1 = \frac{1}{V} \sum_{q_3} \sum_{\Lambda e^{-dl} < q_\perp < \Lambda} \frac{b_2 q_3^2 - m}{\mathcal{E}_n^2 + v^2 q_\perp^2 + (b_2 q_3^2 - m)^2} = \frac{\Lambda^2 dl}{4\pi^2} \int_{-\infty}^{+\infty} dp_3 \frac{b_2 p_3^2 - m}{(v\Lambda)^2 + (b_2 p_3^2 - m)^2} \equiv H_1 dl \quad (14)$$

and

$$\begin{aligned} & \frac{1}{2} \left( \langle S_{1,>}^2 \rangle_{0,>} - \langle S_{1,>} \rangle_{0,>}^2 \right) \\ &= \frac{1}{V} \sum_{\mu=0,1,2,3} \sum_{i\mathcal{E}} \sum_{i\mathcal{E}'} \sum_{\mathbf{p},\mathbf{p}',\mathbf{q}}' F_\mu (\psi_{\alpha,<}^\dagger(\mathbf{p} + \mathbf{q}, i\mathcal{E}) \sigma_\mu \psi_{\alpha,<}(\mathbf{p}, i\mathcal{E})) (\psi_{\alpha,<}^\dagger(\mathbf{p}' - \mathbf{q}, i\mathcal{E}') \sigma_\mu \psi_{\alpha,<}(\mathbf{p}', i\mathcal{E}')) \end{aligned} \quad (15)$$

with

$$F_0 = (h_2 + h_3) \Delta_0^2 + (h_2 + 3h_3) \Delta_0 \Delta_3 + 2(h_2 + h_3) \Delta_0 \Delta_\perp + 2h_2 \Delta_3 \Delta_\perp \quad (16)$$

$$F_3 = h_3 \Delta_0^2 + (-h_2 + 2h_3) \Delta_3^2 + 2h_3 \Delta_\perp^2 + (-h_2 + h_3) \Delta_0 \Delta_3 + 2h_2 \Delta_0 \Delta_\perp + 2(h_2 - h_3) \Delta_3 \Delta_\perp \quad (17)$$

$$F_1 = F_2 = h_2 \Delta_0 \Delta_3 - h_3 \Delta_0 \Delta_\perp + 3h_3 \Delta_3 \Delta_\perp \quad (18)$$

and

$$\begin{aligned} h_2 &= \frac{\Lambda^2 dl}{4\pi^2} \int_{-\infty}^{+\infty} \frac{(v\Lambda)^2 dp_3}{[(v\Lambda)^2 + (b_2 p_3^2 - m)^2]} \equiv H_2 dl, \\ h_3 &= \frac{\Lambda^2 dl}{4\pi^2} \int_{-\infty}^{+\infty} \frac{(b_2 p_3^2 - m)^2 dp_3}{[(v\Lambda)^2 + (b_2 p_3^2 - m)^2]} \equiv H_3 dl. \end{aligned} \quad (19)$$

To evaluate  $h_0, h_1, h_2, h_3$ , we have set the frequencies and momenta for the slow modes (external lines) to zero [10, 12, 20, 21, 31]. After the integration over the fast modes, we scale spatial coordinate, time and field operators as

$$\psi_\alpha = Z_\psi^{-\frac{1}{2}} \psi'_\alpha \equiv e^{-\frac{g dl}{2}} \psi'_\alpha, \quad (20)$$

$$\tau = e^{z dl} \tau', \quad (21)$$

$$\mathbf{x}_\perp = e^{dl} \mathbf{x}'_\perp, \quad (22)$$

$$x_3 = e^{\frac{dl}{2}} x'_3. \quad (23)$$

This leads to one-loop renormalization for  $a, v, b_2, \Delta_0$ ,

$\Delta_3$  and  $\Delta_\perp$ ,

$$a' = a + \left(2 + \frac{1}{2} - g\right) a dl + (\Delta_0 + 2\Delta_\perp + \Delta_3) h_0, \quad (24)$$

$$v' = v + \left(1 + \frac{1}{2} + z - g\right) v dl, \quad (25)$$

$$b'_2 = b_2 + \left(1 + \frac{1}{2} + z - g\right) b_2 dl, \quad (26)$$

$$m' = m + \left(2 + \frac{1}{2} + z - g\right) m dl + (\Delta_0 - 2\Delta_\perp + \Delta_3) h_1, \quad (27)$$

$$\Delta'_0 = \Delta_0 + \left(2 + \frac{1}{2} + 2z - 2g\right) \Delta_0 dl + F_0, \quad (28)$$

$$\Delta'_3 = \Delta_3 + \left(2 + \frac{1}{2} + 2z - 2g\right) \Delta_3 dl + F_3, \quad (29)$$

$$\Delta'_\perp = \Delta_\perp + \left(2 + \frac{1}{2} + 2z - 2g\right) \Delta_\perp dl + F_\perp. \quad (30)$$

We choose a scaling of the field operator  $g$  and dynamical exponent  $z$  in a way that a gapless part of the effective action ( $a, v$  and  $b_2$  in eq. (6)) is invariant under the renormalization [10, 12, 20, 21, 31];

$$g = \left(2 + \frac{1}{2}\right) + (\Delta_0 + 2\Delta_\perp + \Delta_3) H_0, \quad (31)$$

$$z = 1 + (\Delta_0 + 2\Delta_\perp + \Delta_3) H_0. \quad (32)$$

Using this, we obtain from eqs. (27,28,29,30) one-loop renormalization group equations for mass ( $m$ ) and three kinds of disorder strength;

$$\frac{dm}{dl} = m + (\Delta_0 - 2\Delta_\perp + \Delta_3)H_1, \quad (33)$$

$$\frac{d\Delta_0}{dl} = -\frac{1}{2}\Delta_0 + (H_2 + H_3)(\Delta_0 + 2\Delta_\perp + \Delta_3)\Delta_0 + 2H_3\Delta_0\Delta_3 + 2H_2\Delta_3\Delta_\perp, \quad (34)$$

$$\frac{d\Delta_\perp}{dl} = -\frac{1}{2}\Delta_\perp + H_2\Delta_0\Delta_3 - H_3\Delta_0\Delta_\perp + 3H_3\Delta_3\Delta_\perp, \quad (35)$$

$$\frac{d\Delta_3}{dl} = -\frac{1}{2}\Delta_3 + (-H_2 + H_3)(\Delta_0 - 2\Delta_\perp + \Delta_3)\Delta_3 + H_3(\Delta_0^2 + 2\Delta_\perp^2 + \Delta_3^2) + 2H_2\Delta_0\Delta_\perp, \quad (36)$$

To make the RG analysis to be a controlled analysis, Roy et.al. proposed to replace  $b_2(-i)^2\partial_3^2$  in eqs. (5,8) by  $b_n(-i)^n\partial_3^n$  [31]. This leads to replacements of  $b_2p_3^2$  in eqs. (13,14,19) by  $b_np_3^n$  and  $\frac{1}{2}$  in eqs. (23,24,...,31,34,...,36) by  $\frac{1}{n}$ . Thereby, disorder strength of any non-trivial fixed point becomes on the order of  $1/n$  in a large  $n$  limit, which always justifies the above perturbative derivation of the RG equation in the leading order of  $1/n$ . All the scaling analyses based on the RG equation around such fixed points become controlled in the large  $n$  limit. For general even integer  $n$ , we have

$$H_0 = \frac{\Lambda^2}{4\pi^2} \int_{-\infty}^{+\infty} dX \frac{1}{(v\Lambda)^2 + (b_n X^n - m)^2} = \frac{\Lambda^2 R^{\frac{1}{n}-2}}{4\pi^2 b_n^{\frac{1}{n}}} \frac{2\pi \sin[(n-1)\phi_n]}{n \sin[n\phi_n]} \frac{1}{\sin[\frac{\pi}{n}]}, \quad (37)$$

$$H_1 = \frac{\Lambda^2}{4\pi^2} \int_{-\infty}^{+\infty} dX \frac{b_n X^n - m}{(v\Lambda)^2 + (b_n X^n - m)^2} = \frac{\Lambda^2 R^{\frac{1}{n}-1}}{4\pi^2 b_n^{\frac{1}{n}}} \frac{2\pi \sin[\phi_n] + \cos[n\phi_n] \sin[(n-1)\phi_n]}{n \sin[n\phi_n]} \frac{1}{\sin[\frac{\pi}{n}]}, \quad (38)$$

$$H_2 = \frac{\Lambda^2}{4\pi^2} \int_{-\infty}^{+\infty} dX \frac{(v\Lambda)^2}{[(v\Lambda)^2 + (b_n X^n - m)^2]^2} = \frac{\Lambda^2 R^{\frac{1}{n}-2}}{4\pi^2 b_n^{\frac{1}{n}}} \frac{\pi}{n \sin[\frac{\pi}{n}]} \left( \frac{\sin[(n-1)\phi_n]}{\sin[n\phi_n]} - \frac{n-1}{n} \cos[(2n-1)\phi_n] \right), \quad (39)$$

$$H_3 = \frac{\Lambda^2}{4\pi^2} \int_{-\infty}^{+\infty} dX \frac{(b_n X^n - m)^2}{[(v\Lambda)^2 + (b_n X^n - m)^2]^2} = \frac{\Lambda^2 R^{\frac{1}{n}-2}}{4\pi^2 b_n^{\frac{1}{n}}} \frac{\pi}{n \sin[\frac{\pi}{n}]} \left( \frac{\sin[(n-1)\phi_n]}{\sin[n\phi_n]} + \frac{n-1}{n} \cos[(2n-1)\phi_n] \right). \quad (40)$$

with  $H_2 + H_3 \equiv H_0$ .  $n\phi_n$  measures an angle subtended by the mass  $m$  and cutoff energy  $v\Lambda$  (see Fig. 7).

### large- $n$ limit

In the large  $n$  limit, the leading order contribution of  $H_0, H_1, H_2, H_3$  are as follows,

$$H_0 = \frac{\Lambda^2 R^{\frac{1}{n}-2}}{4\pi^2 b_n^{\frac{1}{n}}} \left\{ 2 + \mathcal{O}(n^{-1}) \right\}, H_1 = \frac{\Lambda^2 R^{\frac{1}{n}-1}}{4\pi^2 b_n^{\frac{1}{n}}} \left\{ -\frac{2m}{R} + \mathcal{O}(n^{-1}) \right\},$$

$$H_2 = \frac{\Lambda^2 R^{\frac{1}{n}-2}}{4\pi^2 b_n^{\frac{1}{n}}} \left\{ \frac{2(v\Lambda)^2}{R^2} + \mathcal{O}(n^{-1}) \right\}, H_3 = \frac{\Lambda^2 R^{\frac{1}{n}-2}}{4\pi^2 b_n^{\frac{1}{n}}} \left\{ \frac{2m^2}{R^2} + \mathcal{O}(n^{-1}) \right\}.$$

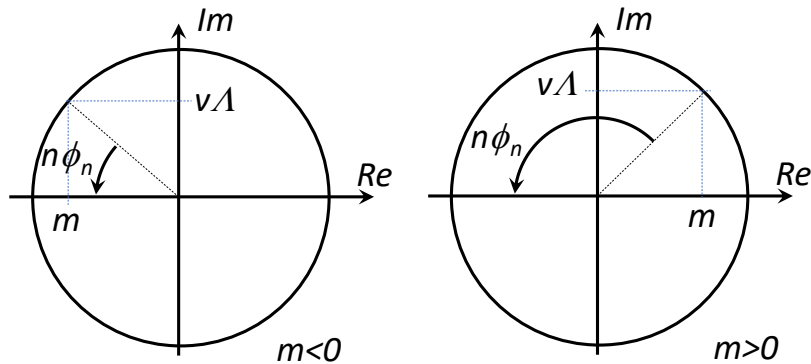


FIG. 7. (color online)  $n\phi_n$  is an angle subtended by the mass  $m$  and cutoff energy  $v\Lambda$  with  $\cos[n\phi_n] = -\frac{m}{R}$  and  $R = \{m^2 + (v\Lambda)^2\}^{\frac{1}{2}}$ . (Left)  $m < 0$ , (Right)  $m > 0$ .

The RG equations in the large  $n$  limit take form of

$$z = 1 + 2(\bar{\Delta}_0 + 2\bar{\Delta}_\perp + \bar{\Delta}_3), \quad (41)$$

$$\frac{dm}{dl} = m - 2m(\bar{\Delta}_0 - 2\bar{\Delta}_\perp + \bar{\Delta}_3) \left(\frac{v\Lambda}{R}\right)^{2-\frac{1}{n}}, \quad (42)$$

$$\frac{d\bar{\Delta}_0}{dl} = -\frac{1}{n}\bar{\Delta}_0 + 2(\bar{\Delta}_0 + 2\bar{\Delta}_\perp + \bar{\Delta}_3)\bar{\Delta}_0 \left(\frac{v\Lambda}{R}\right)^{2-\frac{1}{n}} + 4\bar{\Delta}_0\bar{\Delta}_3 \left(\frac{m}{R}\right)^2 \left(\frac{v\Lambda}{R}\right)^{2-\frac{1}{n}} + 4\bar{\Delta}_3\bar{\Delta}_\perp \left(\frac{v\Lambda}{R}\right)^{4-\frac{1}{n}}, \quad (43)$$

$$\frac{d\bar{\Delta}_\perp}{dl} = -\frac{1}{n}\bar{\Delta}_\perp + 2\bar{\Delta}_0\bar{\Delta}_3 \left(\frac{v\Lambda}{R}\right)^{4-\frac{1}{n}} - 2\bar{\Delta}_0\bar{\Delta}_\perp \left(\frac{m}{R}\right)^2 \left(\frac{v\Lambda}{R}\right)^{2-\frac{1}{n}} + 6\bar{\Delta}_3\bar{\Delta}_\perp \left(\frac{m}{R}\right)^2 \left(\frac{v\Lambda}{R}\right)^{2-\frac{1}{n}}, \quad (44)$$

$$\begin{aligned} \frac{d\bar{\Delta}_3}{dl} = & -\frac{1}{n}\bar{\Delta}_3 + 2(\bar{\Delta}_0 - 2\bar{\Delta}_\perp + \bar{\Delta}_3)\bar{\Delta}_3 \frac{m^2 - (v\Lambda)^2}{R^2} \left(\frac{v\Lambda}{R}\right)^{2-\frac{1}{n}} \\ & + 2(\bar{\Delta}_0^2 + 2\bar{\Delta}_\perp^2 + \bar{\Delta}_3^2) \left(\frac{m}{R}\right)^2 \left(\frac{v\Lambda}{R}\right)^{2-\frac{1}{n}} + 4\bar{\Delta}_0\bar{\Delta}_\perp \left(\frac{v\Lambda}{R}\right)^{4-\frac{1}{n}}, \end{aligned} \quad (45)$$

with  $R^2 \equiv m^2 + (v\Lambda)^2$  and

$$\bar{\Delta}_\mu \equiv \Delta_\mu \cdot \frac{(v\Lambda)^{\frac{1}{n}}}{4\pi^2 v^2 b_n^{\frac{1}{n}}}. \quad (46)$$

In the leading order expansion in large  $n$ , we can replace  $(v\Lambda/R)^{2-\frac{1}{n}}$  and  $(v\Lambda/R)^{4-\frac{1}{n}}$  in the right hand sides of eqs. (42,43,44,45) by  $(v\Lambda/R)^2$  and  $(v\Lambda/R)^4$  respectively. Note also that the RG equations differ from RG equations obtained by Roy et. al. [31] in several aspects. First of all, (i)  $-2m$  in eq. (42) is  $+m$  in the RG equations by Roy et. al. [31], (ii)  $2(\bar{\Delta}_0 + 2\bar{\Delta}_\perp + \bar{\Delta}_3)$  in eq. (41) is  $\bar{\Delta}_0 + 2\bar{\Delta}_\perp + \bar{\Delta}_3$  in Roy et. al. [31] These differences change the scaling exponent of  $m$  and a dynamical exponent  $z$  respectively as well as the density of states scaling around the quantum multicritical point (see the next section for the density of states scaling). Besides, we keep  $m/R$  to be finite, instead of setting  $m/R$  and  $\Lambda/R$  to be zero and unit respectively [31].

The set of RG equations above have only one non-trivial fixed point and a trivial fixed point;

$$\text{FP0 : } (z, m, \bar{\Delta}_0, \bar{\Delta}_\perp, \bar{\Delta}_3) = (1, 0, 0, 0, 0), \quad (47)$$

$$\text{FP1 : } (z, m, \bar{\Delta}_0, \bar{\Delta}_\perp, \bar{\Delta}_3) = \left(1 + \frac{1}{n}, 0, \frac{1}{2n}, 0, 0\right). \quad (48)$$

These two fixed points are on a plane of  $\bar{\Delta}_3 = \bar{\Delta}_\perp = 0$ . Besides, any points in the plane of  $\Delta_3 = \Delta_\perp = 0$  flows within the same plane. The former fixed point is a saddle point of the RG flow, around which the RG equations are linearized as

$$\frac{dm}{dl} = m, \quad \frac{d\Delta_0}{dl} = -\frac{1}{n}\Delta_0. \quad (49)$$

The latter fixed point is an unstable point of the RG flow, around which linearized equations take forms of

$$\frac{dm}{dl} = \left(1 - \frac{1}{n}\right)m, \quad \frac{d\Delta_0}{dl} = \frac{1}{n}\left(\Delta_0 - \frac{1}{2n}\right). \quad (50)$$

### in the case of $n = 2$

For a complementary information, we also analyze the RG equations in the case of  $n = 2$ , where

$$\begin{aligned} H_0 &= \frac{\Lambda^2 R^{\frac{1}{2}-2} \pi}{4\pi^2 b_2^{\frac{1}{2}}} \frac{1}{2 \cos[\phi_2]}, \quad H_1 = \frac{\Lambda^2 R^{\frac{1}{2}-1}}{4\pi^2 b_2^{\frac{1}{2}}} \pi \cos[\phi_2], \\ H_2 &= \frac{\Lambda^2 R^{\frac{1}{2}-2} \pi}{4\pi^2 b_2^{\frac{1}{2}}} \frac{1}{4} \left\{ \frac{1}{\cos[\phi_2]} - \cos[3\phi_2] \right\}, \\ H_3 &= \frac{\Lambda^2 R^{\frac{1}{2}-2} \pi}{4\pi^2 b_2^{\frac{1}{2}}} \frac{1}{4} \left\{ \frac{1}{\cos[\phi_2]} + \cos[3\phi_2] \right\}. \end{aligned}$$

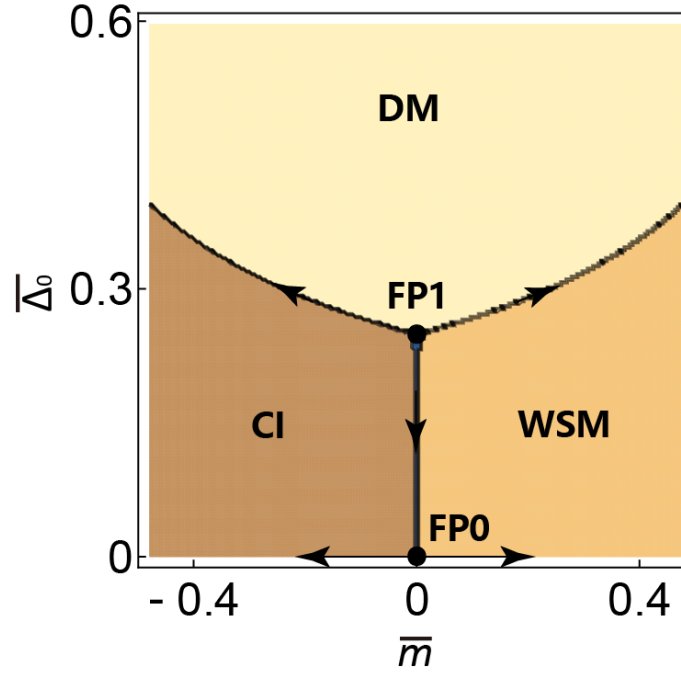


FIG. 8. (color online) Phase diagram in  $\bar{m}$ - $\bar{\Delta}_0$  plane determined by the RG equations in the large  $n$  limit.

A set of the RG equations is simplified as follows,

$$z = 1 + 2(\bar{\Delta}_0 + 2\bar{\Delta}_\perp + \bar{\Delta}_3) \left(\frac{v\Lambda}{R}\right)^{2-\frac{1}{2}} x, \quad (51)$$

$$\frac{dm}{dl} = m + 4R(\bar{\Delta}_0 - 2\bar{\Delta}_\perp + \bar{\Delta}_3) \left(\frac{v\Lambda}{R}\right)^{2-\frac{1}{2}} y, \quad (52)$$

$$\frac{d\bar{\Delta}_0}{dl} = -\frac{1}{2}\bar{\Delta}_0 + 2(\bar{\Delta}_0 + 2\bar{\Delta}_\perp + \bar{\Delta}_3)\bar{\Delta}_0 \left(\frac{v\Lambda}{R}\right)^{2-\frac{1}{2}} x + 2\bar{\Delta}_0\bar{\Delta}_3 \left(\frac{v\Lambda}{R}\right)^{2-\frac{1}{2}} (x+z) + 2\bar{\Delta}_3\bar{\Delta}_\perp \left(\frac{v\Lambda}{R}\right)^{2-\frac{1}{2}} (x-z), \quad (53)$$

$$\frac{d\bar{\Delta}_\perp}{dl} = -\frac{1}{2}\bar{\Delta}_\perp + \bar{\Delta}_0\bar{\Delta}_3 \left(\frac{v\Lambda}{R}\right)^{2-\frac{1}{2}} (x-z) - \bar{\Delta}_0\bar{\Delta}_\perp \left(\frac{v\Lambda}{R}\right)^{2-\frac{1}{2}} (x+z) + 3\bar{\Delta}_3\bar{\Delta}_\perp \left(\frac{v\Lambda}{R}\right)^{2-\frac{1}{2}} (x+z), \quad (54)$$

$$\begin{aligned} \frac{d\bar{\Delta}_3}{dl} = & -\frac{1}{2}\bar{\Delta}_3 + 2(\bar{\Delta}_0 - 2\bar{\Delta}_\perp + \bar{\Delta}_3)\bar{\Delta}_3 \left(\frac{v\Lambda}{R}\right)^{2-\frac{1}{2}} z \\ & + (\bar{\Delta}_0^2 + 2\bar{\Delta}_\perp^2 + \bar{\Delta}_3^2) \left(\frac{v\Lambda}{R}\right)^{2-\frac{1}{2}} (x+z) + 2\bar{\Delta}_0\bar{\Delta}_\perp \left(\frac{v\Lambda}{R}\right)^{2-\frac{1}{2}} (x-z), \end{aligned} \quad (55)$$

with  $R^2 \equiv m^2 + (v\Lambda)^2$ ,  $m/R = -\cos[2\phi_2]$ ,  $v\Lambda/R = \sin[2\phi_2]$  and,

$$\bar{\Delta}_\mu \equiv \Delta_\mu \frac{\pi}{4} \frac{(v\Lambda)^{\frac{1}{2}}}{4\pi^2 v^2 b_2^{\frac{1}{2}}}, \quad x \equiv \frac{1}{\cos[\phi_2]}, \quad y \equiv \cos[\phi_2], \quad z \equiv \cos[3\phi_2]. \quad (56)$$

The set of the RG equations have two non-trivial fixed points and one trivial fixed points;

$$\text{FP0} : \left( z, \frac{m}{R}, \bar{\Delta}_0, \bar{\Delta}_\perp, \bar{\Delta}_3 \right) = (1, 0, 0, 0, 0) \quad (57)$$

$$\text{FP1} : \left( z, \frac{m}{R}, \bar{\Delta}_0, \bar{\Delta}_\perp, \bar{\Delta}_3 \right) = (1.41, -0.447, 0.137, 0.0128, 0.0440) \quad (58)$$

$$\text{FP2} : \left( z, \frac{m}{R}, \bar{\Delta}_0, \bar{\Delta}_\perp, \bar{\Delta}_3 \right) = (1.43, -0.753, 0.0, 0.0, 0.376). \quad (59)$$

Here FP0 and FP1 correspond to FP0 and FP1 in the large- $n$  limit respectively. The trivial fixed point is a

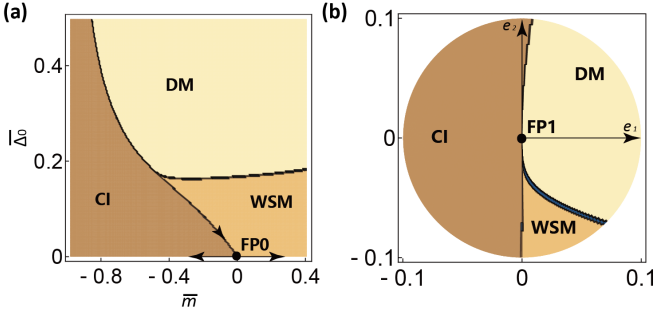


FIG. 9. (color online) (a) Phase diagram in the  $\bar{m}-\bar{\Delta}_0$  plane determined by the RG equations in the case of  $n = 2$ . (b) Phase diagram around FP1 in a plane subtended by  $e_1$  and  $e_2$ .

saddle point of the RG flows, around which the linearized equations take forms of

$$\frac{dm}{dl} = m, \quad \frac{d\bar{\Delta}_\mu}{dl} = -\frac{1}{2}\bar{\Delta}_\mu, \quad (60)$$

with  $\mu = 0, \perp, 3$ . The fixed point FP1 is a saddle point, which determines the criticality of the quantum multicritical point among the DM, WSM, and CI phases. Namely, linearized RG equations around FP1 have two linear-independent directions in a four-dimensional parameter space,  $m-\bar{\Delta}_0-\bar{\Delta}_\perp-\bar{\Delta}_3$  space, along which the RG flow always goes into FP1, and has two other linear-independent directions, along which the RG flow always runs away from FP1. Let us call the latter two directions as  $e_1$  and  $e_2$ . These two belong to eigenvalues  $\lambda_1 = +1.14^*$  and  $\lambda_2 = +0.287^*$  respectively. When an initial parameter set of  $(m, \bar{\Delta}_0, \bar{\Delta}_\perp, \bar{\Delta}_3)$  is slightly deviated from FP1 along  $\pm e_1$ , the corresponding RG flow goes to the DM/CI phase fixed points respectively (See Fig. 9(b)). When an initial set is deviated from FP1 along  $\pm e_2$ , the flow goes to CI/WSM phase fixed points respectively (See Fig. 9(b)). FP2 is an unstable point of the RG flow; linearized RG equations around FP2 have four linear-independent directions, along which the RG flow always runs away from FP2.

### DENSITY OF STATES SCALING IN CROSSOVER REGIMES

A scaling theory of the density of states (DOS) proposed by Kobayashi et.al. [15] is characterized by dynamical exponent  $z$ , critical exponent  $\nu$  and spatial dimension  $d$ . As above, there exist a number of fixed points in a phase diagram of disordered LCI. Every fixed point has different critical and dynamical exponents. To see how the DOS scaling changes along a quantum critical line which connects two fixed points with different exponents, let us first give a general idea of the DOS scaling in the framework of the renormalization group analysis.

### around saddle-point fixed point

Consider a DOS scaling around a saddle-point fixed point, which has one relevant scaling variable  $t$  and one irrelevant scaling variable  $x$  (See Fig. 10(a)). Around the fixed point, these two scaling variables, single-particle energy and spatial length are scaled as follows,

$$\begin{aligned} t' &= b^{-y_t}t, \\ x' &= b^{-y_x}x = b^{|y_x|}x, \\ \xi' &= b\xi, \\ \mathcal{E}' &= b^{-z}\mathcal{E}, \end{aligned}$$

with  $y_t > 0$  and  $y_x < 0$ . Variables with prime in the left hand side are variables after a renormalization, and those without prime in the right hand side are variables before the renormalization;  $b = e^{-dl} < 1$ . When the scaling is spatially isotropic, a volume is scaled by  $b^d$  ( $d$  is a spatial dimension). Thereby, a total number of single-particle states below a given energy  $\mathcal{E}$  per unit volume  $N(\mathcal{E}, t, x)$  is scaled by  $b^{-d}$  under the renormalization;

$$N'(\mathcal{E}', t', x') = b^{-d}N(\mathcal{E}, t, x).$$

Taking a derivative with respect to the energy  $\mathcal{E}$ , we obtain a scaling of the density of states under the renormalization,

$$b^{d-z}\rho'(b^{-z}\mathcal{E}, b^{-y_t}t, b^{-y_x}x) = \rho(\mathcal{E}, t, x), \quad (61)$$

with  $\rho \equiv dN/d\mathcal{E}$ .

To address ourselves to a scaling property of DOS near a critical point, take  $t$  to be very small while  $x$  is not. Suppose that we renormalize many times, such that  $b^{-y_t}t = 1$  ( $b < 1$ ,  $y_t > 0$ ). Solving  $b$  in favor for  $t$ , we have,

$$\rho(\mathcal{E}, t, x) = t^{-\frac{z-d}{y_t}}\rho'(t^{-\frac{z}{y_t}}\mathcal{E}, 1, t^{\frac{|y_x|}{y_t}}x).$$

$t$  is sufficient small, so that the third argument is very tiny. Thus, we have,

$$\begin{aligned} \rho(\mathcal{E}, t, x) &\simeq t^{-\frac{z-d}{y_t}}\rho'(t^{-\frac{z}{y_t}}\mathcal{E}, 1, 0) \\ &\equiv t^{-\frac{z-d}{y_t}}\Phi(t^{-\frac{z}{y_t}}\mathcal{E}). \end{aligned} \quad (62)$$

Noting that  $\xi = at^{-\frac{1}{y_t}}$  (where  $a$  is an atomic length scale), we reach the same DOS scaling theory by Kobayashi et. al. [15].

$$\rho(\mathcal{E}, t, x) = \xi^{z-d}\Phi(\xi^z\mathcal{E}). \quad (63)$$

In the presence of finite strength of the irrelevant scaling variable ( $x \neq 0$ ), the above DOS scaling is valid when

$$x \ll t^{-\frac{|y_x|}{y_t}}. \quad (64)$$

Our lattice model is characterized by microscopic parameters such as the disorder strength  $W$  and an inter-layer coupling strength  $\beta$ . Suppose that there is a saddle-point fixed point which controls a critical property of a

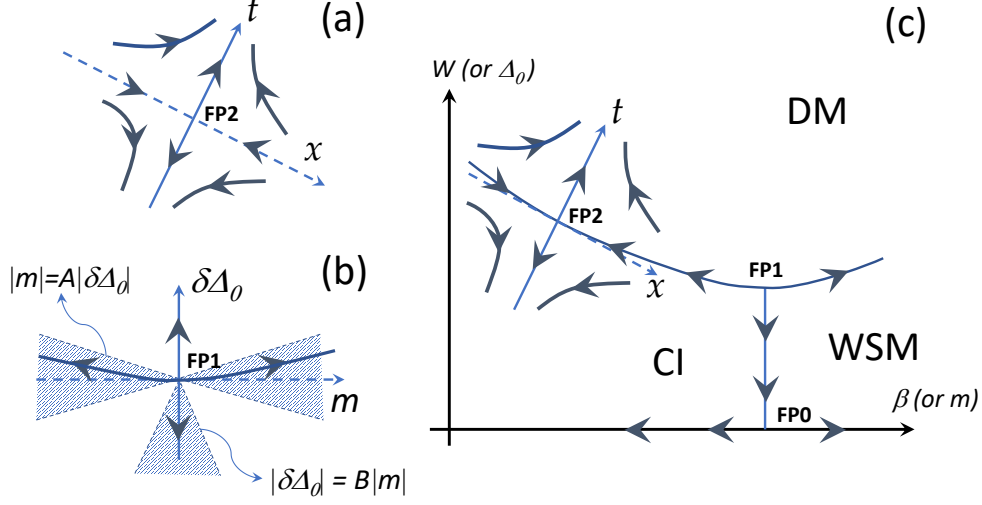


FIG. 10. (color online) Schematic RG phase diagrams. (a) RG phase diagram around saddle-point fixed point (FP2) with one relevant scaling variable  $t$  and one irrelevant scaling variable  $x$ . (b) RG phase diagram around the unstable fixed point FP1 with crossover boundaries.  $|m| = A|\delta\Delta_0|$  denotes a crossover boundary between the DOS scaling given by eq. (71) and that given by eqs. (62,67).  $|\delta\Delta_0| = B|m|$  denotes a crossover boundary between the DOS scaling given by eq. (75) and that given by eq. (77). (c) postulated RG phase diagram with FP0, FP1, and FP2 in a two-dimensional parameter space subtended by the disorder strength  $W$  (or  $\Delta_0$ ) and interlayer coupling strength  $\beta$  (or  $m$ ). We assume that there exists a saddle-point fixed point (named as FP2), which controls the DOS scaling between CI phase with zero zDOS and CI phase with finite zDOS.

phase transition between CI phase with zero zDOS and CI phase with finite zDOS (See Fig. 10(c)). In the two-dimensional parameter space subtended by  $W$  and  $\beta$ , the fixed point has one relevant scaling variable  $t$  and one irrelevant scaling variable  $x$ , both of which are functions of  $W$  and  $\beta$ . The phase boundary between the two CI phases,  $W_{c,1}(\beta)$ , is determined by

$$t(W_{c,1}(\beta), \beta) = 0. \quad (65)$$

For a given  $\beta$ , we can expand  $t(W, \beta)$  in small  $W - W_{c,1}(\beta)$ :

$$\begin{aligned} t(W, \beta) &= \left. \left( \frac{\partial t}{\partial W} \right) \right|_{W=W_{c,1}(\beta)} \cdot (W - W_{c,1}(\beta)) + \dots \\ &\equiv a(\beta) \cdot (W - W_{c,1}(\beta)) + \dots \end{aligned} \quad (66)$$

Substituting this expansion into eq. (62), we obtain the following scaling form for the density of states as a function of  $W$  and  $\mathcal{E}$ ,

$$\begin{aligned} \rho(\mathcal{E}, W, \beta) &= (a(\beta)|W - W_{c,1}(\beta)|)^{-\frac{z-d}{y_t}} \\ &\times \Phi\left((a(\beta)|W - W_{c,1}(\beta)|)^{-\frac{z}{y_t}} \mathcal{E}\right), \end{aligned} \quad (67)$$

for  $W \simeq W_{c,1}(\beta)$  and arbitrary  $\beta$ . Fig. 11(a,b) show a single-parameter scaling plot for DOS as a function of the single-particle energy  $\mathcal{E}$  for  $W > W_{c,1}$  and that for  $W < W_{c,1}$  respectively. Fig. 11(a) demonstrates that, when being plotted according to eq. (67) with  $(d-z)/y_t = 2$  and

$z/y_t = 1$ , DOS for different  $\beta$ ,  $\mathcal{E}$  and  $W > W_{c,1}$  are all fit into a single-parameter function. The observation implies the presence of a saddle-point fixed point (schematically depicted as FP2 in Fig. 10(c)), which controls the DOS scaling between CI with zero zDOS and CI with finite zDOS. Meanwhile, Fig. 11(b) shows that, for the CI with finite energy gap ( $W < W_{c,1}$ ), the data streams for  $\beta = 0.3$  and those for  $\beta = 0.2$  deviate from each other especially when  $\mathcal{E}\delta^{-z/y_t}$  becomes smaller. These data points are from those single-particle states which are proximate (and greater than) the energy gap  $\Delta$ . We speculate that the deviation results from a non-analytic feature of  $\rho(\mathcal{E})$  at  $\mathcal{E} = \Delta$ ,  $\rho(\mathcal{E}) = \theta(\mathcal{E} - \Delta)(\mathcal{E} - \Delta)^{\frac{d-z}{y_t}}$ , and is rather generic in CI with finite energy gap.

#### around the unstable fixed point

Consider next the DOS scaling around the unstable fixed point FP1 in the RG phase diagram of Fig. 8,  $(\overline{\Delta}_0, m) = (\frac{1}{2n}, 0) \equiv (\overline{\Delta}_{0,c}, 0)$ . The FP1 has two relevant scaling variables,  $\delta\overline{\Delta}_0 \equiv \overline{\Delta}_0 - \overline{\Delta}_{0,c}$  and  $m$ ;

$$\begin{aligned} \delta\overline{\Delta}_0' &= b^{-y_\Delta} \delta\overline{\Delta}_0, \\ m' &= b^{-y_m} m, \end{aligned}$$

with  $y_\Delta > 0$  and  $y_m > 0$ . As above, we begin with a scaling relation of the density of states,

$$\rho(\mathcal{E}, \delta\overline{\Delta}_0, m) = b^{\frac{5}{2}-z} \rho'(b^{-z}\mathcal{E}, b^{-y_\Delta}\delta\overline{\Delta}_0, b^{-y_m}m). \quad (68)$$

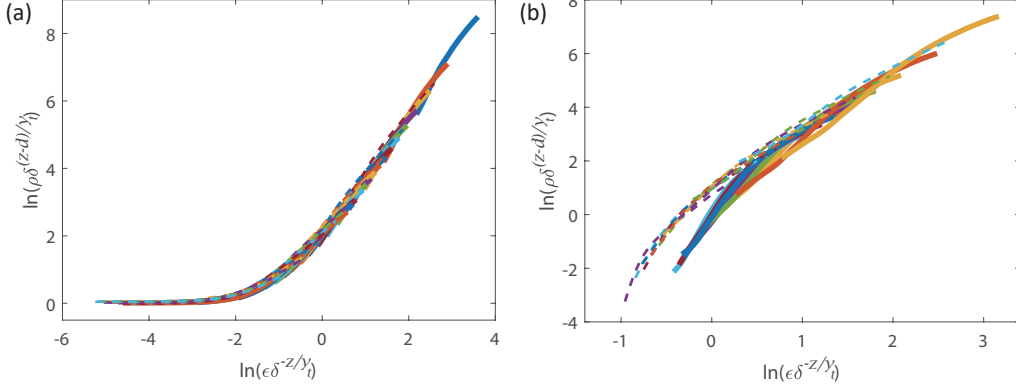


FIG. 11. (color online) Single-parameter scaling of the density of states for  $\beta = 0.2$  (solid lines) and  $\beta = 0.3$  (dotted lines) for different disorder strength  $W$  near the transition point between CI phase with zero zDOS and CI phase with finite zDOS; (a)  $W > W_{c,1}$  (b)  $W < W_{c,1}$ . Only those data points with  $\rho(E) > 0.008/0.004$  are used for the plot for  $\beta = 0.2/0.3$  in (a) and  $\rho(E) > 0.001$  for (b). We use eq. (67) for the scaling fit with  $(d-z)/y_t = 2$  and  $z/y_t = 1$ . In the fitting for  $\beta = 0.2$  and  $\beta = 0.3$ , we use the same  $a(\beta)$  in eq. (67).

Here we replaced  $b^d$  in eq. (61) by  $b^{\frac{5}{2}}$ , because a volume is scaled by  $b^{\frac{1}{2}+1+1}$  under the anisotropic scaling given in eqs. (20,21,22,23). Firstly consider that the system approaches FP1 along a line of  $m = 0$  (along a line named as “(1)” in Fig. 12(a)). Using the same argument as above, we obtain the DOS scaling along  $m = 0$ ,

$$\begin{aligned} \rho(\mathcal{E}, \delta\bar{\Delta}_0, 0) &= (\delta\bar{\Delta}_0)^{-\frac{2z-5}{2y_\Delta}} \rho'((\delta\bar{\Delta}_0)^{-\frac{z}{y_\Delta}} \mathcal{E}, 1, 0) \\ &\equiv (\delta\bar{\Delta}_0)^{-\frac{2z-5}{2y_\Delta}} \Phi'((\delta\bar{\Delta}_0)^{-\frac{z}{y_\Delta}} \mathcal{E}). \end{aligned} \quad (69)$$

According to the large- $n$  analyses in the previous section, we have

$$z = 1 + \frac{1}{n}, \quad y_\Delta = \frac{1}{n}, \quad y_m = 1 - \frac{1}{n} \quad (70)$$

For  $n = 2$ , we thus evaluate the DOS scaling function as

$$\rho(\mathcal{E}, \delta\bar{\Delta}_0, 0) = (\delta\bar{\Delta}_0)^2 \Phi'((\delta\bar{\Delta}_0)^{-3} \mathcal{E}). \quad (71)$$

In the presence of finite  $m$ , the DOS scaling near a critical line of  $\delta\bar{\Delta}_0 = 0$  such as a critical line between CI with zero zDOS and CI with finite zDOS (along a line named as “(2)” in Fig. 12(a)) or a critical line between DM and WSM phases (along a line named as “(3)” in Fig. 12(a)) is controlled *not* by FP1. Instead it is controlled by the other saddle-point fixed points which we assume to exist in finite  $m$  region such as FP2 schematically depicted in Fig. 10(c). A crossover between these two different DOS scalings is determined by the two relevant scaling variables at FP1,  $y_\Delta$  and  $y_m$ . To see this, we compare the DOS at small  $\delta\bar{\Delta}_0$  and DOS at  $\delta\bar{\Delta}'_0 \equiv b^{-y_\Delta} \delta\bar{\Delta}_0 = 1$ . From eq. (68), these two are related by,

$$\begin{aligned} \rho(\mathcal{E}, \delta\bar{\Delta}_0, m) &= (\delta\bar{\Delta}_0)^{-\frac{2z-5}{2y_\Delta}} \\ &\times \rho'((\delta\bar{\Delta}_0)^{-\frac{z}{y_\Delta}} \mathcal{E}, 1, (\delta\bar{\Delta}_0)^{-\frac{y_m}{y_\Delta}} m). \end{aligned} \quad (72)$$

When the third argument in eq. (72) is much smaller than 1, the DOS scaling follows the same scaling form at  $m = 0$ , i. e. eq. (71). When the third argument is much greater than 1, the DOS scaling is determined by the other fixed point. Thus, a crossover between these two DOS scalings occurs around

$$|m| = A |\delta\bar{\Delta}_0|^{\frac{y_m}{y_\Delta}}. \quad (73)$$

(see Fig. 10(b)). From eq. (70), this crossover line is given by  $m = A |\delta\bar{\Delta}_0|$  for  $n = 2$ .

### DOS scaling for CI-WSM branch

In the phase diagram subtended by  $W$  and  $\beta$  (or  $\bar{\Delta}_0$  and  $m$  respectively), CI phase and WSM phase are intervened by the quantum critical line which connects FP0 and FP1. The RG flow between these two dictates that the critical property as well as the DOS scaling in the critical line is controlled by the scaling property at FP0 [31]. Thereby,  $m$  and  $\bar{\Delta}_0$  are scaled by

$$\begin{aligned} \bar{\Delta}'_0 &= b^{-y_\Delta} \bar{\Delta}_0, \\ m' &= b^{-y_m} m, \end{aligned}$$

where  $y_\Delta = -\frac{1}{2}$  ( $n = 2$ ),  $y_m = 1$ , and  $z = 1$ . To determine the DOS scaling for CI-WSM branch ( $\bar{\Delta}_0 < \bar{\Delta}_{0,c}$ ), we begin with a comparison between the DOS at very small  $m$  and DOS at  $m' = b^{-y_m} m = 1$ ;

$$\begin{aligned} \rho(\mathcal{E}, \bar{\Delta}_0, m) &= b^{\frac{5}{2}-z} \rho'(b^{-z} \mathcal{E}, b^{-y_\Delta} \bar{\Delta}_0, b^{-y_m} m) \\ &= m^{-\frac{2z-5}{2y_m}} \rho'(m^{-\frac{z}{y_m}} \mathcal{E}, m^{-\frac{y_\Delta}{y_m}} \bar{\Delta}_0, 1) \end{aligned} \quad (74)$$

When  $m$  is tiny, so is the second argument in eq. (74). This leads to the following DOS scaling for CI-WSM

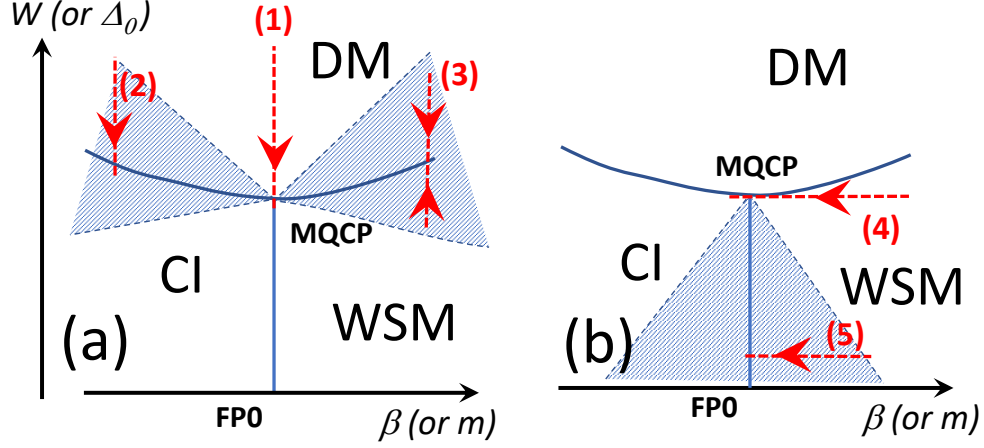


FIG. 12. (color online) DOS scalings around the quantum multicritical point (equivalent to the unstable fixed point called as FP1 in Fig. 8). Boundary lines between the blue shaded regions and the other regions stand for crossover boundaries between different critical regimes. (a)  $\rho(E, t) = t^{-\frac{d-z}{y_t}} \Psi(t^{-\frac{z}{y_t}} \mathcal{E})$  with  $t \equiv |W - W_{c,1}|$  for lines of (2) and (3).  $\rho(E, t) = t^{-\frac{5-2z}{2y_t}} \Psi(t^{-\frac{z}{y_t}} \mathcal{E})$  with  $t \equiv |W - W_{c,1}|$  for a line of (1). (b)  $\rho(E, m) = m^{-\frac{5-2z}{2y_m}} \Psi(m^{-\frac{z}{y_m}} \mathcal{E})$  with  $m \equiv |\beta - \beta_c|$ . (1)  $(5 - 2z)/(2y_t) = 2$ ,  $z/y_t = 3$ . (2)  $(d - z)/y_t = 2$ ,  $z/y_t = 1$ . (3)  $(d - z)/y_t = 1.23$ ,  $z/y_t = 1.29$  [adopted from Ref. [25]]. (4)  $(5 - 2z)/(2y_m) = 2$ ,  $z/y_m = 3$ . (5)  $(5 - 2z)/(2y_m) = 3/2$ ,  $z/y_m = 1$ .

branch;

$$\begin{aligned} \rho(\mathcal{E}, \bar{\Delta}_0, m) &= m^{-\frac{2z-5}{2y_m}} \Psi(m^{-\frac{z}{y_m}} \mathcal{E}) \\ &= m^{\frac{3}{2}} \Psi(m^{-1} \mathcal{E}), \end{aligned} \quad (75)$$

for  $\bar{\Delta}_0 < \bar{\Delta}_{0,c}$ . From the second line to the third line, we put values of  $y_m$  and  $z$  at FP0. Meanwhile, exactly at  $\bar{\Delta}_0 = \bar{\Delta}_{0,c}$ , the DOS scaling is controlled by the scaling property at FP1. To determine the DOS scaling at  $\bar{\Delta}_0 = \bar{\Delta}_{0,c}$ , we compare the DOS at small  $m$  and that at  $m' = e^{-y_m} m = 1$  in eq. (68) with  $\delta \bar{\Delta}_0 = 0$ . The comparison gives out

$$\begin{aligned} \rho(\mathcal{E}, \delta \bar{\Delta}_0 = 0, m) &= m^{-\frac{2z-5}{2y_m}} \rho'(m^{-\frac{z}{y_m}} \mathcal{E}, 0, 1) \\ &\equiv m^{-\frac{2z-5}{2y_m}} \Psi'(m^{-\frac{z}{y_m}} \mathcal{E}). \end{aligned} \quad (76)$$

where  $y_m$  and  $z$  are scaling dimension of  $m$  and dynamical exponent at FP1 respectively. For  $n = 2$ , this in combination with eq. (70) leads to the following evaluation of the DOS scaling at  $\bar{\Delta}_0 = \bar{\Delta}_{0,c}$ ,

$$\rho(\mathcal{E}, \bar{\Delta}_0 = \bar{\Delta}_{0,c}, m) = m^2 \Psi'(m^{-3} \mathcal{E}). \quad (77)$$

The crossover between eq. (75) and eq. (77) occurs at

$$|\bar{\Delta}_0 - \bar{\Delta}_{0,c}| = B|m|^{\frac{y_{\Delta}}{y_m}} \quad (78)$$

For  $n = 2$ , this crossover boundary can be evaluated as  $|\bar{\Delta}_0 - \bar{\Delta}_{0,c}| = B|m|$  (Fig. 10(b)).

### POLYNOMIAL FITTING OF CI-DM BRANCH

For those data points in Fig. 2, the polynomial fitting results give  $W_c = 2.21$ , while we could see by eye that

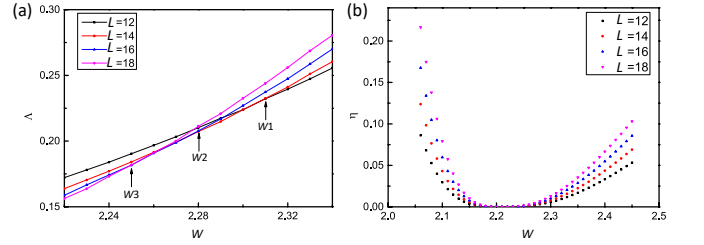


FIG. 13. (color online) (a) Enlarged figure of Fig. 2 around  $W_c$ .  $W_1, W_2, W_3$  denote an intersection point between  $L=12$ , and 14, that between  $L = 14$  and 16, that between  $L = 16$  and 18 respectively. (b) Ratio between the 3rd order term and a sum of the lower order terms in the polynomial fitting with  $(m_1, m_2, n_1, n_2) = (2, 0, 3, 1)$ ,  $\eta$  given in eq. (79), as a function of the disorder strength  $W$  for different system size  $L$ .

the intersection of curves with different  $L$  occur at  $W_c = 2.27$  in Fig. 2. Fig. 13(a) is an enlarged figure of Fig. 2. From this, one can see that the intersection of curves with larger size moves in the direction of smaller  $W$ , being consistent with the polynomial fitting result ( $W_c = 2.21$ ).

A convergence of the polynomial fitting results with  $(m_1, m_2, n_1, n_2) = (2, 0, 3, 1)$  for the data points in Fig. 2 is demonstrated in Fig. 13(b). The figure shows a ratio between the 3rd order term and a sum of the lower order terms:

$$\eta \equiv \frac{a_{3,0} \phi_1^3}{a_{0,0} + a_{1,0} \phi_1 + a_{2,0} \phi_1^2}. \quad (79)$$

One can see that the ratio is already tiny (below 8%)

near the critical disorder  $W_c$  ( $2.1 < W < 2.4$ ). This indicates that the polynomial fitting with  $(m_1, m_2, n_1, n_2) = (2, 0, 3, 1)$  is convergent.

---

\* rshindou@pku.edu.cn

- [1] S. Murakami, *New Journal of Physics* **9**, 356 (2007).
- [2] L. Balents, ‘Weyl electrons kiss’, *Physics* **4**, 36 (2011).
- [3] S.-Y. Xu, I. Belopolski, N. Alidoust, M. Neupane, G. Bian, C. Zhang, R. Sankar, G. Chang, Z. Yuan, C.-C. Lee, S.-M. Huang, H. Zheng, J. Ma, D. S. Sanchez, B. K. Wang, F.-C. Bansil, A.; Chou, P. P. Shibayev, H. Lin, S. Jia, and M. Z. Hasan, *Science* **349**, 613 (2015).
- [4] B. Q. Lv, H. M. Weng, B. B. Fu, X. P. Wang, J. Miao, Ma, P. Richard, X. C. Huang, L. X. Zhao, G. F. Chen, Z. Fang, X. Dai, T. Qian, and H. Ding, *Phys. Rev. X* **5**, 031013 (2015).
- [5] X. Wan, A. M. Turner, A. Vishwanath, and S. Y. Savrasov, *Phys. Rev. B* **83**, 205101 (2011).
- [6] H. Weng, C. Fang, Z. Fang, B. A. Bernevig, and X. Dai, *Phys. Rev. X* **5**, 011029 (2015).
- [7] X. Huang, L. Zhao, Y. Long, P. Wang, C. Chen, Z. Yang, H. Liang, M. Xue, H. Weng, Z. Fang, X. Dai, and G. Chen, *Phys. Rev. X* **5**, 031023 (2015).
- [8] A. A. Burkov and L. Balents, *Phys. Rev. Lett.* **107**, 127205 (2011).
- [9] M. Vazifeh and M. Franz, *Phys. Rev. Lett.* **111**, 027201 (2013).
- [10] E. Fradkin, *Phys. Rev. B* **33**, 3263 (1986).
- [11] R. Shindou and S. Murakami, *Physical Review B* **79**, 045321 (2009).
- [12] P. Goswami and S. Chakravarty, *Phys. Rev. Lett.* **107**, 196803 (2011).
- [13] S. Ryu and K. Nomura, *Physical Review B* **85**, 155138 (2012).
- [14] K. Kobayashi, T. Ohtsuki, and K.-I. Imura, *Phys. Rev. Lett.* **110**, 236803 (2013).
- [15] K. Kobayashi, T. Ohtsuki, K.-I. Imura, and I. F. Herbut, *Phys. Rev. Lett.* **112**, 016402 (2014).
- [16] Y. Ominato and M. Koshino, *Phys. Rev. B* **89**, 054202 (2014).
- [17] R. Nandkishore, D. A. Huse, and S. L. Sondhi, *Phys. Rev. B* **89**, 245110 (2014).
- [18] B. Sbierski, G. Pohl, E. J. Bergholtz, and P. W. Brouwer, *Phys. Rev. Lett.* **113**, 026602 (2014).
- [19] B. Roy and S. Das Sarma, *Phys. Rev. B* **90**, 241112 (2014).
- [20] S. V. Syzranov, V. Gurarie, and L. Radzihovsky, *Phys. Rev. B* **91**, 035133 (2015).
- [21] S. V. Syzranov, L. Radzihovsky, and V. Gurarie, *Phys. Rev. Lett.* **114**, 166601 (2015).
- [22] J. H. Pixley, P. Goswami, and S. Das Sarma, *Phys. Rev. Lett.* **115**, 076601 (2015).
- [23] B. Sbierski, E. J. Bergholtz, and P. W. Brouwer, *Phys. Rev. B* **92**, 115145 (2015).
- [24] C.-Z. Chen, J. Song, H. Jiang, Q.-f. Sun, Z. Wang, and X. C. Xie, *Phys. Rev. Lett.* **115**, 246603 (2015).
- [25] S. Liu, T. Ohtsuki, and R. Shindou, *Phys. Rev. Lett.* **116**, 066401 (2016).
- [26] H. Shapourian and T. L. Hughes, *Phys. Rev. B* **93**, 075108 (2016).
- [27] S. Bera, J. D. Sau, and B. Roy, *Phys. Rev. B* **93**, 075108 (2016).
- [28] B. Roy and S. Das Sarma, *Phys. Rev. B* **93**, 119911 (2016).
- [29] S. V. Syzranov, P. M. Ostrovsky, L. Radzihovsky, and V. Gurarie, *Phys. Rev. B* **93**, 155113 (2016).
- [30] J. H. Pixley, D. A. Huse, and S. Das Sarma, *Phys. Rev. X* **6**, 021042 (2016).
- [31] B. Roy, R.-J. Lager, and J. Vladimir, arXiv:1610.08973 (2016).
- [32] Y. Su, X. S. Wang, and X. R. Wang, arXiv:1701.00905 (2017).
- [33] K. Slevin and T. Ohtsuki, *Phys. Rev. Lett.* **78**, 4083 (1997).
- [34] T. Kawarabayashi, B. Kramer, and T. Ohtsuki, *Phys. Rev. B* **57**, 11842 (1998).
- [35] K. Slevin and T. Ohtsuki, *Journal of the Physical Society of Japan* **85**, 104712 (2016).
- [36] S. Hikami, A. I. Larkin, and Y. Nagaoka, *Progress of Theoretical Physics* **63**, 707 (1980).
- [37] K. B. Effetov, A. I. Larkin, and D. E. Khmel'nitsukii, *Soviet Phys. JETP* **52**, 568 (1980).
- [38] F. Evers and A. D. Mirlin, *Rev. Mod. Phys.* **80**, 1355 (2008).
- [39] See Supplemental Materials for details of the two-orbital tight-binding model, perturbative renormalization group analyses on the effective continuum model, density of states scalings around the quantum multicritical point, a localization-delocalization transition point for the CI-DM branch, and convergence of the polynomial fitting analyses for the CI-DM branch.
- [40] A. MacKinnon, and B. Kramers, *Phys. Rev. Lett.* **47**, 1546 (1981).
- [41] J. L. Pichard and G. Sarma, *J. Phys.* **C14**, L127 (1981).
- [42] K. Slevin and T. Ohtsuki, *Phys. Rev. Lett.* **82**, 382 (1999).
- [43] K. Slevin and T. Ohtsuki, *New Journal of Physics* **16**, 015012 (2014).
- [44] K. Slevin, T. Ohtsuki, and T. Kawarabayashi, *Phys. Rev. Lett.* **84**, 3915 (2000).
- [45] A. Weiße, G. Wellein, A. Alvermann, and H. Fehske, *Rev. Mod. Phys.* **78**, 275 (2006).
- [46] Altland, Alexander and Simons, Ben, *Condensed Matter Field Theory* (2010, Cambridge University Press).